Tilted double Dirac cone and anisotropic quantum-spin-Hall topological insulator in mechanical granular graphene

Li-Yang Zheng, Georgios Theocharis, Romain Fleury, Vincent Tournat, Vitali Goussev

▶ **To cite this version:**

Li-Yang Zheng, Georgios Theocharis, Romain Fleury, Vincent Tournat, Vitali Goussev. Tilted double Dirac cone and anisotropic quantum-spin-Hall topological insulator in mechanical granular graphene. New Journal of Physics, 2020, 22 (10), pp.103012. 10.1088/1367-2630/abb862 . hal-03448813

HAL Id: hal-03448813
https://hal.science/hal-03448813

Submitted on 25 Nov 2021

HAL is a multi-disciplinary open access archive for the deposit and dissemination of scientific research documents, whether they are published or not. The documents may come from teaching and research institutions in France or abroad, or from public or private research centers.

L'archive ouverte pluridisciplinaire **HAL**, est destinée au dépôt et à la diffusion de documents scientifiques de niveau recherche, publiés ou non, émanant des établissements d'enseignement et de recherche français ou étrangers, des laboratoires publics ou privés.

New Journal of Physics
The open access journal at the forefront of physics

Deutsche Physikalische Gesellschaft DPG IOP Institute of Physics

PAPER • OPEN ACCESS

Tilted double Dirac cone and anisotropic quantum-spin-Hall topological insulator in mechanical granular graphene

To cite this article: Li-Yang Zheng *et al* 2020 *New J. Phys.* **22** 103012

View the article online for updates and enhancements.

You may also like

- Silicene on substrates: A theoretical perspective
Hong-Xia Zhong, , Ru-Ge Quhe et al.
- Dirac fermions in blue-phosphorus
Yuanchang Li and Xiaobin Chen
- Tunable Dirac cones in single-layer selenium
Zhendong Chen, Yuefang Hu, Ziming Zhu et al.

This content was downloaded from IP address 195.221.243.139 on 25/11/2021 at 12:23

New Journal of Physics
The open access journal at the forefront of physics

Deutsche Physikalische Gesellschaft DPG
IOP Institute of Physics

Published in partnership with: Deutsche Physikalische Gesellschaft and the Institute of Physics

OPEN ACCESS

RECEIVED
23 June 2020

REVISED
26 August 2020

ACCEPTED FOR PUBLICATION
14 September 2020

PUBLISHED
7 October 2020

Original content from this work may be used under the terms of the Creative Commons Attribution 4.0 licence.

Any further distribution of this work must maintain attribution to the author(s) and the title of the work, journal citation and DOI.

PAPER

Tilted double Dirac cone and anisotropic quantum-spin-Hall topological insulator in mechanical granular graphene

Li-Yang Zheng[1], Georgios Theocharis[1,*], Romain Fleury[2], Vincent Tournat[1] and Vitalyi Gusev[1]

[1] Laboratoire d'Acoustique de l'Université du Mans (LAUM), UMR 6613, Institut d'Acoustique - Graduate School (IA-GS), CNRS, Le Mans Université, France
[2] Laboratory of Wave Engineering, Ecole Polytechnique Fédérale de Lausanne (EPFL), 1015 Lausanne, Switzerland
[*] Author to whom any correspondence should be addressed.

E-mail: georgiostheocharis@gmail.com

Keywords: topological insulator, quantum spin Hall effect, tilted double Dirac cone

Abstract

Dirac degeneracies are essential ingredients to control topological charge exchanges between bands and trigger the unique edge transport properties of topological materials. In addition, when Dirac cones are tilted, exotic phenomena can emerge such as anomalous Hall effect or unconventional Klein tunneling. However, the unique topological transport properties arising from the opening of tilted Dirac cone degeneracies have been left completely uncharted. Here, we demonstrate a new form of Dirac degeneracy that occurs in mechanical granular graphene (MGG): a tilted double Dirac cone, composed of two counter-tilted type-I Dirac cones. Different from the reported C_6 systems, we show that the tilted double Dirac cone is present in a C_2 granular graphene. Remarkably, a pair of anisotropic helical edge waves appears when the degeneracy is lifted. This leads to an anisotropic quantum spin-Hall topological insulator that possesses unique wave propagation properties, including anisotropic edge dispersion and direction-dependent edge-bulk mode conversion.

1. Introduction

In topological materials, the existence of edge/surface states is induced by the topology of bulk bands [1–5]. A non-trivial topology is typically acquired through the lifting of a point degeneracy between bands, such as the one stemming from a linear band crossing (Dirac cone) in momentum space. The crossing point is termed Dirac point (or Weyl point in three-dimensional spin-non-degenerate systems) [6–8]. The presence of Dirac cones, as commonly seen in graphene or graphene-like structures, is protected by time-reversal symmetry (TRS) and inversion symmetry. Breaking the TRS leads to quantum Hall effect [9] while breaking the inversion symmetry results in quantum valley Hall phase [10]. Moreover, keeping the TRS and inversion symmetry, Dirac cones can be lifted by the intrinsic spin–orbit coupling (SOC). In this case, the topological materials, called Z_2 topological insulators, exhibit the so-called quantum spin Hall (QSH) phase [11–13] and robust helical edge states. Similar phenomena have also been investigated in classical photonic/phononic/mechanical systems. There, effective spin degeneracy has been emulated using double Dirac cones (overlap of two Dirac cones), allowing for the observation of classical analogs to QSH effects [14–21].

Dirac cones can be tilted due to, for example, mechanical deformation [22], external magnetic fields [23] or anisotropic hoppings [24]. In this case, the zero-energy Fermi surface can take different shapes, depending on the strength of the tilt [25–27]. In type-I tilted Dirac cone, the strength of the tilt is relatively weak, thus the Fermi surface remains a point (the Dirac point). Examples include the hydrogenated graphene [28], organic semiconductor [29] and type-I Weyl semimetals [30]. When the strength of the tilt is strong, a type-II Dirac cone emerges with the Fermi surface turning into two lines crossing at the Dirac point. This dispersion has been reported in type-II Dirac and Weyl semimetals [31–34], screw symmetry

© 2020 The Author(s). Published by IOP Publishing Ltd on behalf of the Institute of Physics and Deutsche Physikalische Gesellschaft

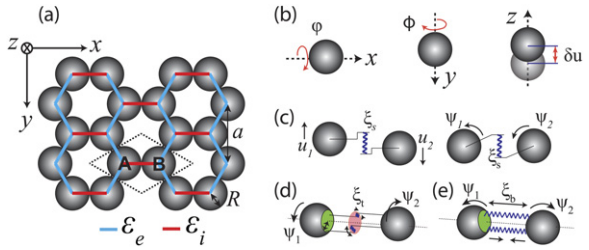

Figure 1. (a) Schematic view of the MGG. The black dash box highlights a unit cell. The red (blue) bonds represent internal-couplings ε_i (external-couplings ε_e). (b) Possible movements of individual particles in the MGG. Schematic presentation of shear (c), torsional (d) and bending (e) interactions between two adjacent particles.

photonic crystals [35], graphyne-like lattices [36] and metasurfaces [37]. Recently, a type-III Dirac cone is demonstrated in different systems [38–40], where the Fermi surface is a single line at the critical transition from a point-like (type-I) to a lines-crossing (type-II) Fermi surface. The successful implementation of different kinds of Dirac cones could open the door for advanced control of waves [41–43]. In particular, manipulation of tilted Dirac cones could bring drastically different transport phenomena. For example, in type-I tilted Weyl metals with broken TRS, anomalous Hall effect can be observed [44, 45]. Moreover, in some Dirac materials, the anisotropic property due to tilted energy dispersions leads to the unconventional Klein tunneling [46, 47].

However, the physical properties of tilted double Dirac cones, i.e. a fourfold degeneracy obtained at the band touching points between two counter-tilted (opposite tilting angle) Dirac cones, have been left completely unexplored. This is due to the difficulty in obtaining such degeneracies. The requirement of extra hopping/deformation lowers the symmetry of structures, typically preventing these complex forms of symmetry-protected Dirac cones to occur in low symmetry lattices [48]. Yet, tilted double Dirac cones may bring novel wave physics and an unique form of Dirac/Weyl semimetals. Exploring this new area rises fundamental questions that must be answered. For example, how to obtain a tilted double Dirac cone in a simple lattice? Once the tilted Dirac degeneracy is lifted by SOC, would a novel form of QSH effect appear? And if yes what is the influence of the tilt on the properties of the helical edge states?

In this work, we answer the above questions, demonstrating a novel form of anisotropic QSH effect. We first demonstrate how to form a tilted double Dirac cone in a modified mechanical granular graphene (MGG) under out-of-plane motion excitation [figure 1(a)]. One of the key ingredients is that the MGG, in which each bead possesses one translational and two rotational degrees of freedom (DOFs) [49–52], provides sufficient number of modes for a fourfold degeneracy. This is the key for a tilted double Dirac cone in a C_2 symmetry lattice, which is completely distinguished from the band-folding technique on C_6 structures [19, 53]. Another key ingredient is the existence of rotations which play a significant role as providing two pairs of rotational degenerate modes at the Brillouin zone (BZ) center. In the presence of two in-plane rotations, a double Dirac cone can be achieved by tuning the rigidities. Interestingly, when modifications are introduced which lower the symmetry of the MGG from C_6 to C_2, the existence of the double Dirac dispersion is not affected due to the accidental nature of the degeneracy. However, the modifications lead to a novel type of Dirac dispersion: a tilted double Dirac cone. We show that lifting the Dirac degeneracy can introduce a Z_2 band gap, which supports a pair of topological helical edge modes. We further demonstrate the transport properties of the anisotropic spin-locked helical edge waves. Our results as well as the recent experimental studies confirm the relevance of MGG as a reliable platform to study novel Dirac and topological wave physics reported here [54, 55].

2. Model

The MGG, a two-dimensional (2D) monolayer granular crystal, is shown in figure 1(a). Considering the out-of-plane motion, each bead exhibits one out-of-plane translation u and two in-plane rotations φ, ϕ (with respect to the x- and y- axes, respectively) i.e., figure 1(b). The movements of individual particles lead to the following forces and/or interactions: (1) shear forces with the rigidity ξ_s (figure 1(c)); (2) torsional moments with the rigidity ξ_t (figure 1(d)); (3) bending moments with the rigidity ξ_b (figure 1(e)). For simplicity, we set $\xi_t = \xi_b$, and denote them as $\eta_b = \eta_t = \varepsilon_e$, where $\eta_{b,t} = \xi_{b,t}/\xi_s$ are the ratios of bending/torsional rigidities to shear rigidity. Each unit cell (highlighted by black dash box) can be viewed as a molecule with internal-couplings ε_i (red bonds) within the molecule, and with external-couplings ε_e (blue bonds) to its neighbors.

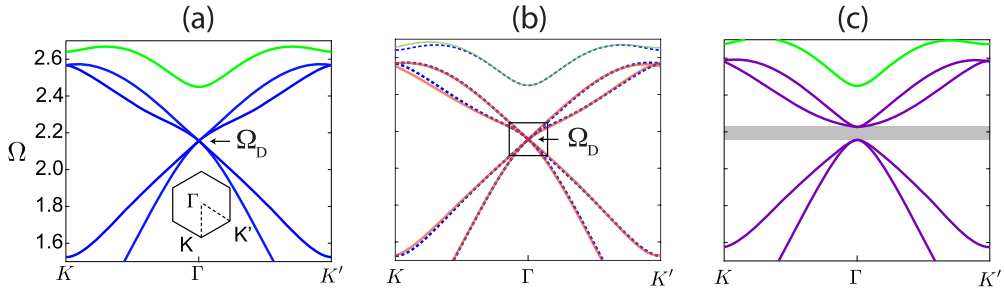

Figure 2. Dispersion curves for (a) $\varepsilon_e = \varepsilon_i = 0.5$, (b) $\varepsilon_e = 0.45, \varepsilon_i = 0.6$, and (c) $\varepsilon_e = 0.5, \varepsilon_i = 0.6$. A double Dirac cone appears in (a) and (b) at the Dirac frequency Ω_D. The inset of (a) shows the Brillouin zone. The dashed lines in (b) correspond to the dispersion in (a).

By analyzing the motions between beads related to the unit cell and applying the Bloch wave solution, a dynamical equation of the MGG is given by (the full derivation can be found in references [54, 55]),

$$\begin{bmatrix} D_1 & D_2 \\ D_2^* & D_1 \end{bmatrix} \boldsymbol{v} = \Omega^2 \boldsymbol{v}, \tag{1}$$

where $\boldsymbol{v} = [u_A; \Phi_A; \Psi_A; u_B; \Phi_B; \Psi_B]$ with $\Phi = R\varphi$, $\Psi = R\phi$ (R is the radius of the beads). $*$ denotes the complex conjugate. $\Omega = \omega\sqrt{M/\xi_s}$ is the normalized frequency, ω is the cyclic frequency. D_1 and D_2 are 3×3 matrices of the following forms,

$$D_1 = \begin{bmatrix} 3 & 0 & 0 \\ 0 & \left(2\varepsilon_e + \varepsilon_i + \frac{3}{2}\right) P & 0 \\ 0 & 0 & \left(2\varepsilon_e + \varepsilon_i + \frac{3}{2}\right) P \end{bmatrix}, \tag{2}$$

$$D_2 = \begin{bmatrix} -(\alpha + 2\beta)/P & \mathrm{i}\gamma/P & (\alpha - \beta)/P \\ -\mathrm{i}\gamma & (1 + l)\beta - \varepsilon_i\alpha & -\mathrm{i}\gamma/2 \\ -(\alpha - \beta) & -\mathrm{i}\gamma/2 & l\beta + (1 - \varepsilon_i)\alpha \end{bmatrix}. \tag{3}$$

Above, $l = (1 - 4\varepsilon_e)/2$, and $\alpha = P\ \mathrm{e}^{-2\mathrm{i}q_x}$, $\beta = P\ \mathrm{e}^{\mathrm{i}q_x}\ \cos q_y$, $\gamma = \sqrt{3}P\ \mathrm{e}^{\mathrm{i}q_x}\ \sin q_y$. $q_x = k_x R$, $q_y = \sqrt{3}k_y R$ are the normalized wave vectors for k_x, k_y, respectively. $P = MR^2/I$ with I the moment of inertia. Normally, $P \in [1.5\ 2.5]$ corresponding to a hollow sphere where all the mass is at the sphere periphery ($P = 1.5$) and a homogeneously filled sphere ($P = 2.5$), respectively. To this end, we set $P = 1.55$.

Equation (1) leads to the $\Omega - k$ dispersion as shown in figure 2(a) when $\varepsilon_i = \varepsilon_e = 0.5$. It can be seen that a double Dirac cone appears at the Dirac frequency $\Omega_D = \sqrt{3P}$ at the Γ point (the BZ center). The four degenerate modes at the Γ point are purely rotational modes. When $\varepsilon_i = \varepsilon_e$, the graphene structure holds a C_{6v} symmetry. An accidental degeneracy of the wave functions corresponding to E_1 and E_2 irreducible representations of the C_{6v} group occurs when $2\varepsilon_e + \varepsilon_i = 3/2$, leading to a double Dirac cone of purely rotational modes at the Γ point. Interestingly, even when the symmetry is reduced to a C_2 by setting $\varepsilon_i = 0.6, \varepsilon_e = 0.45$ [figure 2(b)], the double Dirac cone is preserved at the Γ point since $2\varepsilon_e + \varepsilon_i = 3/2$ is still valid. Although the irreducible representations of the C_2 group are one-dimensional (symmetry or asymmetry), the tilted double Dirac cone is a degeneracy of twofold symmetric and asymmetric modes, see appendix A. In the MGG, the number of pure rotational modes is twice the number of the irreducible representations of C_2, the extra modes of the same nature (rotations) would double the number of wave functions of the same irreducible representations, leading to twofold symmetric and asymmetric modes in the C_2 MGG at the Γ point. By keeping $2\varepsilon_e + \varepsilon_i = 3/2$, accidental degeneracy of the twofold modes occurs again, forming the double Dirac cone. However, the influence of symmetry reduction to C_2 is to tilt each individual Dirac cone in opposite angle with respect to the Dirac point, leading to the tilted double Dirac cone. The full gap by tuning ε_e and ε_i [$\varepsilon_e \neq \varepsilon_i$, figure 2(c)] does not break C_2 symmetry, but destroys the accidental degeneracy, giving rise to a Z_2 topological phase transition of bulk bands accompanying with the band inversion as discussed appendix A.

3. Tilted double Dirac cone

To unveil the bulk properties of the tilted double Dirac cone and derive the effective Hamiltonian in the vicinity of the Dirac point ($\delta\boldsymbol{k} = (\delta k_x, \delta k_y)$), we follow an asymptotic model developed in reference [56]

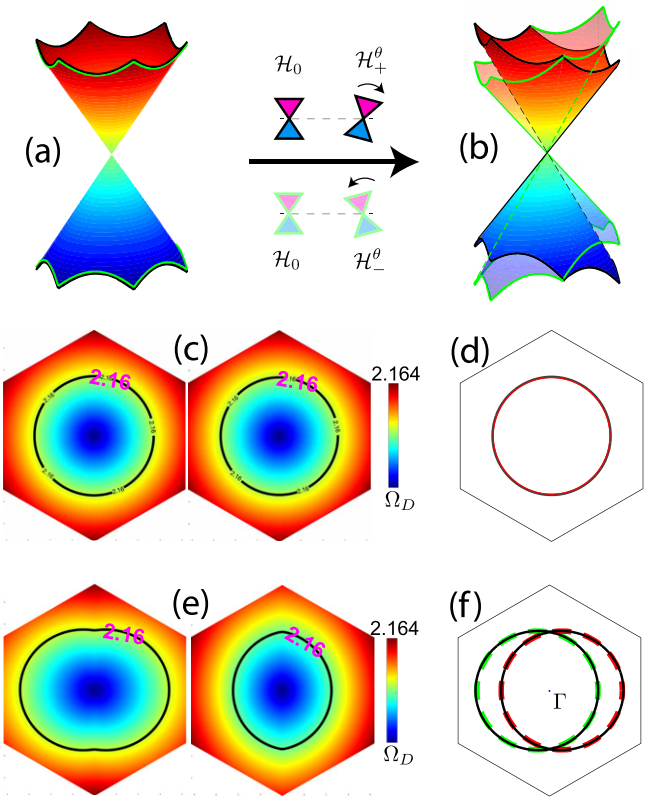

Figure 3. (a) A standard double Dirac cone when $\varepsilon_e = \varepsilon_i = 0.5$. (b) A tilted double Dirac cone when $\varepsilon_e = 0.45, \varepsilon_i = 0.6$. (c) Iso-frequency contours of the upper cones of the untilted Dirac cone in (a). The black curves correspond to the frequency $\Omega = 2.16$. (d) The cross section (black and red curves) by cutting the untilted Dirac cone of (a) at $\Omega = 2.16$. (e) Iso-frequency contours of the upper cones of the tilted Dirac cone in (b). (f) The cross section (black curves) by cutting the tilted Dirac cone of (b) at $\Omega = 2.16$. The red and green dashed ellipses are the predictions of $\mathcal{H}_\pm^\theta$.

(see appendix B). The following dynamical equation is obtained,

$$\begin{bmatrix} \mathcal{H}_0 & m\sigma_z - \mathrm{i}m_s\sigma_0 \\ m\sigma_z + \mathrm{i}m_s\sigma_0 & \mathcal{H}_0 \end{bmatrix} \psi = \Delta\Omega\psi \tag{4}$$

where $\mathcal{H}_0 = V_D\delta\boldsymbol{k}\cdot\boldsymbol{\sigma}$ is a 2×2 Dirac Hamiltonian with the Dirac velocity $V_D = \Omega_D R/4$. $\boldsymbol{\sigma} = (\sigma_x, \sigma_y, \sigma_z)$ are the Pauli matrices and σ_0 is the identity matrix. $\Delta\Omega = \Omega - \Omega_D - m$ where $m = (4\varepsilon_e + 2\varepsilon_i - 3)\Omega_D/12$ denotes the 'effective mass' due to SOC that breaks the degeneracy [54]. $m_s = 4/3 * \varepsilon' V_D\delta k_x$ is a symmetry-breaking mass with the modified parameter $\varepsilon' = \varepsilon_i - \varepsilon_e$. For nonzero δk, it suggests that m_s relies on the propagating direction. The four components spinor $\psi = [\boldsymbol{p}; \boldsymbol{d}]$ consists two circular polarized basis $\boldsymbol{p} = [p_L; p_R] = [\Phi_A + \mathrm{i}\Psi_A; \mathrm{i}\Phi_B + \Psi_B)]/\sqrt{2}$ and $\boldsymbol{d} = [d_L; d_R] = [-(\Phi_B + \mathrm{i}\Psi_B); \mathrm{i}\Phi_A + \Psi_A)]/\sqrt{2}$. 'L/R' represents the left/right circular polarization, which is the pseudo-spin DOF in the MGG. When the accidental degeneracy is valid ($2\varepsilon_e + \varepsilon_i = 3/2$), m is zero. Thus, the fourfold degeneracy is guaranteed at the Γ point no matter the value of m_s, leading to a double Dirac cone in the C_2 MGG. This indicates that the mass m_s is not responsible for the opening of the Dirac cone. In fact, m_s is responsible for the change of is the standard double Dirac cone [figure 3(a)] to tilted one [figure 3(b)]. This can be more easily demonstrated, by transforming the Hamiltonian of equation (4) as follows (see details in appendix B),

$$H_t = \begin{bmatrix} \mathcal{H}_+ & m\sigma_z \\ m\sigma_z & \mathcal{H}_- \end{bmatrix} \tag{5}$$

where $\mathcal{H}_\pm = \pm(4/3 * \varepsilon' V_D)\delta k_x\sigma_0 + V_D(\delta k_x\sigma_x + \delta k_y\sigma_y)$, is the standard tilted Dirac Hamiltonian [23], indicating that two standard Dirac cones are tilted in the x direction to opposite angles denoted by the signs $\pm$. Applying the mass m_s into the Hamiltonian, it reads: $\mathcal{H}_\pm = \pm m_s\sigma_0 + V_D(\delta k_x\sigma_x + \delta k_y\sigma_y)$. It is clear that when $m_s = 0$, $\mathcal{H}_\pm = \mathcal{H}_0$. Therefore, the double Dirac cone is the overlapping of two standard Dirac cones. However, when $m_s \neq 0$, the Dirac cones of $\mathcal{H}_\pm$ are tilted in opposite angles with respect to the Dirac point, leading to the tilted double Dirac cone.

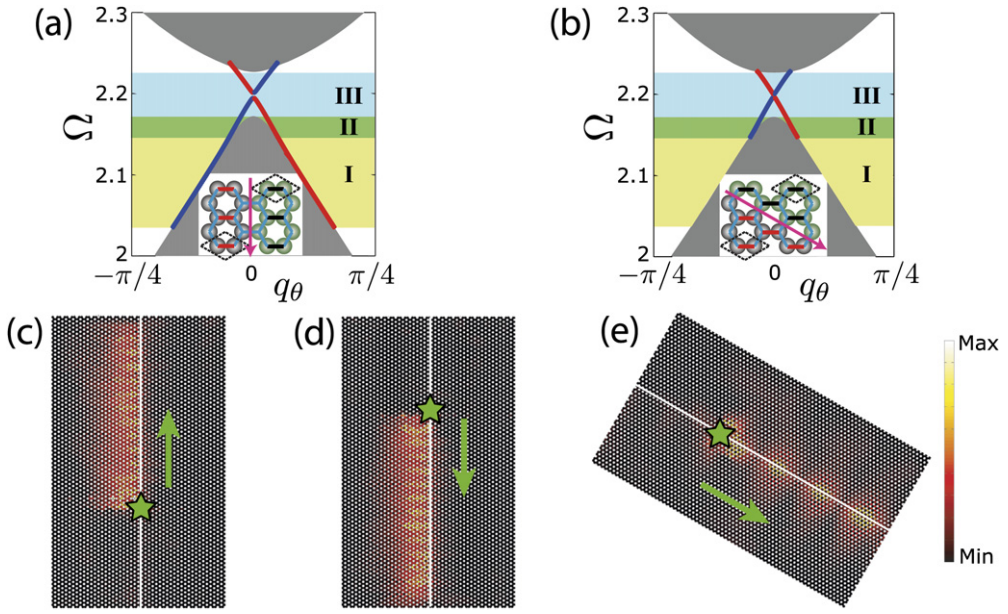

Figure 4. Edge dispersion in (a) the VZI with $\theta = -\pi/2$ (the insert of (a)) and in (b) the IZI with $\theta = -\pi/6$ (the inset of (b)). (c)–(e) Unidirectional transport. The sources are labeled by the stars. The three color areas indicate the different mode-type regions corresponding to figure 5(a).

The tilt parameter defined as $\tilde{v} \equiv \sqrt{\frac{V_x^2+V_y^2}{V_D^2}}$ determines the tilted type of Dirac cone [23]. According to $\mathcal{H}_\pm$, we have $V_x = 4/3 * \varepsilon' V_D$, $V_y = 0$, therefore $\tilde{v} = 4|\varepsilon'|/3$. In this work, we consider $\tilde{v} < 1$, namely the tilted Dirac cones belong to type-I category. However, by tuning ε', other types of tilted double Dirac cone can also be achieved, see appendix C.

Due to the tilting effect, wave behavior around the Dirac point exhibits anisotropic properties. Figure 3(e) shows the iso-frequency contours (IFCs) of the two upper branches of figure 3(b). For comparison, the IFCs of the untilted case [figure 3(a)] are shown in figure 3(c). In both cases, the contours of $\Omega = 2.16$ are marked in black curves as examples. The cross sections by cutting the two upper cones of (a) and (b) at 2.16 are presented in (d) and (f), respectively. It shows that the IFCs of the untilted case are circles, suggesting isotropic property of wave propagation. However, in the C_2 MGG, the IFCs are deformed to complex shapes, resulting in the wave behavior that is highly related to the direction of propagation.

To confirm that the anisotropic properties stem from the tilt, we further simplify the Hamiltonian in equation (5) to a block diagonal form: $[\mathcal{H}_+^\theta, 0; 0, \mathcal{H}_-^\theta]$ with the 2×2 tilted Hamiltonian, see appendix B,

$$\mathcal{H}_\pm^\theta = V_\pm \Delta \boldsymbol{k} \cdot \boldsymbol{\sigma} \pm m\sigma_z. \tag{6}$$

Above, $V_\pm = (1 \pm 4/3 * \varepsilon' \cos\theta) V_D$ is the anisotropic Dirac velocity, and $\theta \in (-\pi, \pi]$ is the angle of wave vector to the x-axis. The tilted Hamiltonian in equation (6) shows that the slope of the linear dispersion ($V_\pm$) around the Dirac point is anisotropic, depending on the propagation angle θ. When $m = 0$, the elegance of $\mathcal{H}_\pm^\theta$ to capture the wave physics around the Dirac point is shown in figure 3(f), where the cross section of the counter-tilted double Dirac cone [obtained from equation (1)] at $\Omega = 2.16$ is presented in black curves. The red and green dashed ellipses correspond to the prediction of $\mathcal{H}_+^\theta$ and $\mathcal{H}_-^\theta$, respectively. The perfect match of the two colored ellipses with the black curves verifies our theory, that is, the Dirac cone of $\mathcal{H}_+^\theta$ (red ellipse) is tilted to the positive x-direction, while $\mathcal{H}_-^\theta$ (green ellipse) to the negative, resulting in the anisotropy around the Dirac point.

It should be mentioned that the Hamiltonian in equation (6) can be rewritten as $\mathcal{H}_\pm^\theta = V_D \delta\tilde{\boldsymbol{k}}_\pm \cdot \boldsymbol{\sigma} \pm m\sigma_z$ where $\delta\tilde{\boldsymbol{k}}_\pm = \delta\boldsymbol{k} + \mathcal{A}_\pm$ with $\mathcal{A}_\pm = \pm 4/3 * \varepsilon' \delta\boldsymbol{k} \cos\theta$. This indicates that the symmetry reduction to C_2 equally introduces a pseudomagnetic field, defined as $\mathcal{B}_\pm = \nabla \times \mathcal{A}_\pm$ as discussed in references [57–59]. However, this reduction does not break TRS because the total pseudomagnetic field of the counter-tilted double Dirac cones, $\mathcal{B} = \mathcal{B}_+ + \mathcal{B}_-$, is zero. See the discussion of TRS in appendix D. Under TRS, the nonzero m due to SOC induces a Z_2 topological phase, leading to a nontrivial topological gap around the Dirac point as discussed in appendix A. Thus, equation (6) is an anisotropic QSH Hamiltonian, formed by two copies of tilted Dirac fermion Hamiltonians $\mathcal{H}_+^\theta$ and $\mathcal{H}_-^\theta$.

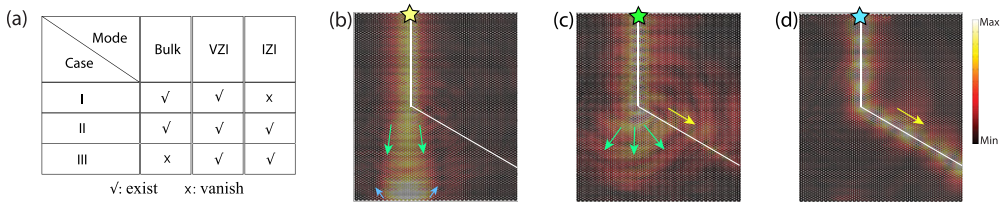

Figure 5. Topological edge-bulk modes conversion. (a) Three cases of mode types that correspond to the color regions in figure 4. (b)–(d) Spatiotemporal simulations of topological transport in (b) case I (yellow in figure 4), in (c) case II (green) and in (d) case III (light blue).

Consequently, equation (6) predicts the existence of a pair of time-reversal edge modes (helical edge waves) with exotic transport properties.

4. Anisotropic quantum spin-Hall effect

The anisotropic QSH Hamiltonian $\mathcal{H}_{\pm}^{\theta}$ supports the unidirectional propagation of topological rotational waves along different interface configurations. As shown in the inserts of figures 4(a) and (b), a vertical zigzag interface (VZI) with $\theta = -\pi/2$ and an inclined zigzag interface (IZI) with $\theta = -\pi/6$ are constructed. We set cyan bonds $\epsilon_e = 0.5$ for both sides, while the red bonds $\varepsilon_i = 0.6$ ($\varepsilon' = 0.1$, gray beads), and the black bonds $\varepsilon_i = 0.4$ ($\varepsilon' = -0.1$, green beads). On the interface, the bonds is equal to 0.5. We also scale down the mass of beads in green by a factor $f = 0.92$ to ensure that a full gap appears around Ω_D. Figures 4(a) and (b) show the edge dispersion. The bulk modes are labeled in gray, and the edge modes are marked by red and blue. More details about the calculation of edge mode spectra can be found in appendix E. It can be seen that the two zigzag interfaces support a pairs of topological edge waves, since the edge waves (red and blue lines) are spin-locked, they support unidirectional transport along the interfaces. As examples, the spatiotemporal evolution of edge waves (propagation of rotation-dominated waves) on the VZI are implemented in figures 4(c) and (d). An interface unit cell is used to be a harmonic source (green star) to excite the eigenmodes in the red or blue branches. The color scale represents the total magnitude of rotation ($|\Phi| + |\Psi|$) in each bead. It shows that the edge wave transport is either upward [figure 4(c)] or downward [figure 4(d)], manifesting the one-way propagation property. The unidirectionality of edge transport along the IZI is demonstrated in figure 4(e), where the helical edge waves propagate solely to the $\theta = -\pi/6$ direction.

As can be seen from figures 4(a) and (b), there is a difference in the edge dispersions along the VZI and the IZI direction. This is translated into distinct wave propagation along these directions. It is reasonable to relate this direction-dependent edge transport with the resulting anisotropic property of the bulk waves around the Dirac point when the condition $2\varepsilon_e + \varepsilon_i = 3/2$ is kept. Once the tilted double Dirac cone is lifted, the edge waves, that appear in the bulk gap, also exhibit such a direction-dependent transport. Thus, we observe an interesting bulk-edge correspondence that 'transfers' the anisotropy character of the underlying bulk waves to the resulting edge waves.

Remarkably, the direction-dependent property of edge wave transport leads to the topological edge-bulk mode conversion in the MGG. To demonstrate, an interface path is constructed by combining the VZI and IZI [inserts of figures 4(a) and (b)]. Thus, a corner appears to connect the VZI and IZI as shown in figure 5. When edge waves are excited from the source (stars), the turning of waves on the corner depends highly on the frequency location of different mode types. As shown in figure 5(a), there are three cases of mode types corresponding to the three colored areas in figures 4(a) and (b). The spatiotemporal evolution of edge waves for the three cases are shown in figures 5(b)–(d), respectively. In case I where topological edge modes do not exist in the IZI [figure 5(b)], the edge waves of the VZI, which are topologically protected, can only transfer to the bulk modes when meet the corner. Therefore, the topological edge waves spread into the bulk and reflect back when bulk waves come to the free edge on the bottom, leading to zero transport of waves along the IZI. In case II [figure 5(c)], since all the three types of modes can exist in the MGG, the edge waves of the VZI can transfer into the bulk and the IZI at the corner, resulting in the spreading of waves into both the bulk and the IZI. In case III [figure 5(d)], due to the fact that the MGG does not support the propagation of bulk modes, i.e., frequencies in the band gap, the edge waves in the VZI transfer only to the IZI at the corner.

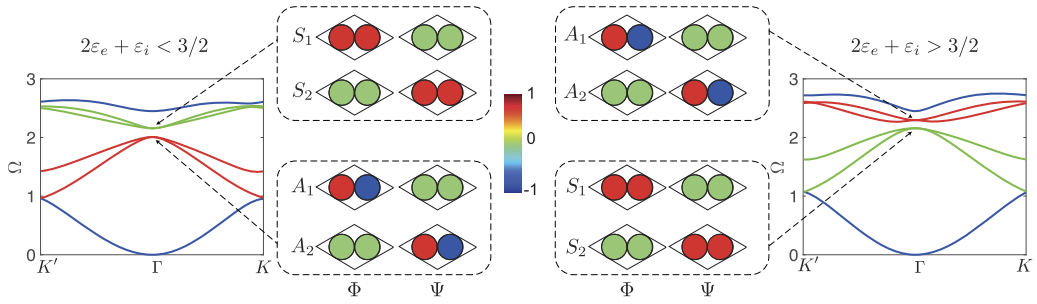

Figure A1. Dispersion curves and the corresponding rotational modes around the tilted Dirac cone for $2\varepsilon_e + \varepsilon_i < 3/2$ (left panel) and for $2\varepsilon_e + \varepsilon_i > 3/2$ (right panel).

5. Conclusions

In this work, we report a tilted double Dirac cone in a C_2 MGG under out-of-plane motion excitation. We found that the bulk dynamics around the Dirac cone is described by an effective anisotropic QSH Hamiltonian, which in contrast with the conventional case, is formed by two copies of the counter-tilted Dirac fermion Hamiltonians. The tilting effect results in a pair of helical edge waves with rich anisotropic transport properties. Our results can stimulate the study of novel Dirac/Weyl materials, and far-reaching applications for beam-splitters, switches and filters.

Acknowledgments

This work was funded by APAMAS project and the project CS.MICRO funded under the program Etoiles Montantes of the Region Pays de la Loire.

Appendix A. Band inversion mechanism

Band inversion occurs in the C_2 MGG by tuning ε_e and ε_i to pass through $2\varepsilon_e + \varepsilon_i = 3/2$. The mechanism is demonstrated in the figure A1. The critical point for the band inversion is exactly the condition for the accidental degeneracy: $2\varepsilon_e + \varepsilon_i = 3/2$. There are two symmetric modes (S_1, S_2) and two asymmetric modes (A_1, A_2) around the Dirac frequency. When $2\varepsilon_e + \varepsilon_i < 3/2$, the two modes of the lower cone are asymmetric modes, while the ones of the upper cone are symmetric. These four modes overlap when $2\varepsilon_e + \varepsilon_i = 3/2$, forming the tilted double Dirac cone. When $2\varepsilon_e + \varepsilon_i > 3/2$, the two modes of the lower cone become the symmetric modes, while the ones of the upper cone become the asymmetric ones. The topological phase transition happens at $2\varepsilon_e + \varepsilon_i = 3/2$.

Appendix B. Hamiltonian of tilted double Dirac cone

At the Γ point, equation (1) predicts four degenerate modes at the Dirac frequency $\Omega_D = \sqrt{3P}$:

$$\mathbf{\Phi}_A = [0;1;0;0;0;0], \quad \mathbf{\Psi}_A = [0;0;1;0;0;0], \quad \mathbf{\Phi}_B = [0;0;0;0;1;0], \quad \mathbf{\Psi}_B = [0;0;0;0;0;1]. \tag{A1}$$

Below, we follow an asymptotic model developed in reference [56] to get the wave dynamical equation around the Dirac point. When k_x, k_y are close to zero and Ω to Ω_D, modes $\boldsymbol{v}$ around the Dirac point can be expressed as the linear combination of those at the Γ point,

$$\boldsymbol{v} = X\boldsymbol{\mu} + \delta\boldsymbol{v}, \|\delta\boldsymbol{v}\| \ll \|\boldsymbol{v}\|, \tag{A2}$$

where $\boldsymbol{\mu} = [\mu_1;\mu_2;\mu_3;\mu_4]$, and $X = [\mathbf{\Phi}_A, \mathbf{\Psi}_A, \mathbf{\Phi}_B, \mathbf{\Psi}_B]$. Similarly, the dynamical matrix can be written as,

$$\mathcal{D} = \mathcal{D}_0 + \delta\mathcal{D}, \tag{A3}$$

where $\delta\mathcal{D} = \eta'\partial_{\eta'}\mathcal{D} + \varepsilon'\partial_{\varepsilon'}\mathcal{D} + \delta k_x\partial_{k_x}\mathcal{D} + \delta k_y\partial_{k_y}\mathcal{D}$ is the first order correction stemming from the small perturbations of η' and ε' in the vicinity of Dirac frequency $\Omega = \Omega_D + \delta\Omega$ ($\|\delta\Omega\| \ll \|\Omega_D\|$) around the Γ point ($\delta k_x, \delta k_y$). Substituting equations (A2) and (A3) to equation (1) and using

$(\Omega_{\rm D}+\delta\Omega)^2 \approx \Omega_{\rm D}^2 + 2\Omega_{\rm D}\delta\Omega$, we arrive at the following equation, by ignoring the second and higher order corrections,

$$\mathcal{D}_0\delta\boldsymbol{v} + \delta\mathcal{D}X\boldsymbol{\mu} = \Omega_{\rm D}^2\delta\boldsymbol{v} + 2\Omega_{\rm D}\delta\Omega X\boldsymbol{\mu}. \tag{A4}$$

By left multiplying the projector $X^\dagger$ to equation (A4), finally we can get the following equation,

$$H\boldsymbol{\mu} = \Delta\Omega\boldsymbol{\mu}, \tag{A5}$$

where the effective Hamiltonian H is given by,

$$H = \begin{bmatrix} 0 & 0 & {\rm i}V_{\rm D}\delta k_x - m + {\rm i}m_{\rm s} & -{\rm i}V_{\rm D}\delta k_y \\ 0 & 0 & -{\rm i}V_{\rm D}\delta k_y & -{\rm i}V_{\rm D}\delta k_x - m + {\rm i}m_{\rm s} \\ -{\rm i}V_{\rm D}\delta k_x - m - {\rm i}m_{\rm s} & {\rm i}V_{\rm D}\delta k_y & 0 & 0 \\ {\rm i}V_{\rm D}\delta k_y & {\rm i}V_{\rm D}\delta k_x - m - {\rm i}m_{\rm s} & 0 & 0 \end{bmatrix}. \tag{A6}$$

Above, $V_{\rm D} = \frac{3PR}{4\Omega_{\rm D}}$, $m_{\rm s} = \frac{4}{3}\varepsilon' V_{\rm D}\delta k_x$, and $\Delta\Omega = \Omega - \Omega_{\rm D} - m$ with $m = \frac{P\eta'}{2\Omega_{\rm D}}$. Equation (A5) describes the wave dynamics around the Γ point near the Dirac frequency. H can be mapped into a Dirac equation, by changing the linear basis of equation (A5) to a circular polarized one:

$$\boldsymbol{\psi} = U\boldsymbol{\mu}, U = \frac{1}{\sqrt{2}}\begin{bmatrix} 1 & {\rm i} & 0 & 0 \\ 0 & 0 & {\rm i} & 1 \\ 0 & 0 & -1 & -{\rm i} \\ {\rm i} & 1 & 0 & 0 \end{bmatrix}. \tag{A7}$$

This circularly polarized spinor basis defines the pseudo-spin in the granular graphene. Under the new basis $\boldsymbol{\psi}$, equation (A5) reads,

$$H_{\rm s}\boldsymbol{\psi} = \begin{bmatrix} \boldsymbol{p} \\ \boldsymbol{d} \end{bmatrix} = \begin{bmatrix} \mathcal{H}_0 & m\sigma_z - {\rm i}m_{\rm s}\sigma_0 \\ m\sigma_z + {\rm i}m_{\rm s}\sigma_0 & \mathcal{H}_0 \end{bmatrix}\begin{bmatrix} \boldsymbol{p} \\ \boldsymbol{d} \end{bmatrix} = \Delta\Omega\begin{bmatrix} \boldsymbol{p} \\ \boldsymbol{d} \end{bmatrix}, \tag{A8}$$

where $\mathcal{H}_0 = V_{\rm D}(k_x\sigma_x + k_y\sigma_y)$ is the Dirac Hamiltonian and the spin basis,

$$\boldsymbol{p} = \begin{bmatrix} p_{\rm L} \\ p_{\rm R} \end{bmatrix} = \begin{bmatrix} \Phi_A + {\rm i}\Psi_A \\ {\rm i}\Phi_B + \Psi_B \end{bmatrix}, \quad \boldsymbol{d} = \begin{bmatrix} d_{\rm L} \\ d_{\rm R} \end{bmatrix} = \begin{bmatrix} -(\Phi_B + {\rm i}\Psi_B) \\ {\rm i}\Phi_A + \Psi_A \end{bmatrix}. \tag{A9}$$

The subscripts L, R represent the left or right circular polarization defined by the unitary matrix U (i.e. equation (A7)) acting on the linear basis $\boldsymbol{\mu}$. The tilting of the Dirac cones can be investigated by applying the following unitary matrix,

$$U' = \frac{1}{\sqrt{2}}\begin{bmatrix} 1 & 0 & -{\rm i} & 0 \\ 0 & 1 & 0 & -{\rm i} \\ -{\rm i} & 0 & 1 & 0 \\ 0 & -{\rm i} & 0 & 1 \end{bmatrix}. \tag{A10}$$

Equation (A8) becomes,

$$H_{\rm t}\boldsymbol{s} = \begin{bmatrix} \mathcal{H}_+ & m\sigma_z \\ m\sigma_z & \mathcal{H}_- \end{bmatrix}\begin{bmatrix} \boldsymbol{s}_+ \\ \boldsymbol{s}_- \end{bmatrix} = \Delta\Omega\begin{bmatrix} \boldsymbol{s}_+ \\ \boldsymbol{s}_- \end{bmatrix} = \Delta\Omega\boldsymbol{s}, \tag{A11}$$

with $\boldsymbol{s} = U'\boldsymbol{\psi}$ and $\mathcal{H}_\pm = \pm V_A\delta k_x\sigma_0 + V_{\rm D}(\delta k_x\sigma_x + \delta k_y\sigma_y)$ the general form of type-I tilted Dirac Hamiltonian. When $m = 0$, $H_{\rm t}$ describes two counter-tilted Dirac cones $\mathcal{H}_\pm$ overlapping at the Dirac point.

By applying the unitary matrix,

$$U'' = \frac{1}{2}\begin{bmatrix} 1 & {\rm e}^{-{\rm i}\theta} & 1 & -{\rm e}^{-{\rm i}\theta} \\ {\rm e}^{{\rm i}\theta} & 1 & -{\rm e}^{{\rm i}\theta} & 1 \\ -1 & {\rm e}^{-{\rm i}\theta} & 1 & {\rm e}^{-{\rm i}\theta} \\ {\rm e}^{{\rm i}\theta} & -1 & {\rm e}^{{\rm i}\theta} & 1 \end{bmatrix}, \tag{A12}$$

where θ satisfies $\delta k_x = |\delta k|\cos\theta, \delta k_y = |\delta k|\sin\theta$, $H_{\rm t}$ can be rewritten as follow,

$$H^\theta = \begin{bmatrix} m & V_+(\delta k_x - {\rm i}\delta k_y) & 0 & 0 \\ V_+(\delta k_x + {\rm i}\delta k_y) & -m & 0 & 0 \\ 0 & 0 & -m & V_-(\delta k_x - {\rm i}\delta k_y) \\ 0 & 0 & V_-(\delta k_x + {\rm i}\delta k_y) & m \end{bmatrix}, \tag{A13}$$

or in a compact form, $H^\theta = [\mathcal{H}_+^\theta, 0; 0, \mathcal{H}_-^\theta]$ with $\mathcal{H}_\pm^\theta = V_\pm(k_x\sigma_x + k_y\sigma_y) \pm m\sigma_z$, and $V_\pm = V_{\rm D}(1 \pm \frac{4}{3}\varepsilon'\ \cos\ \theta)$. The anisotropic basis is $\boldsymbol{s}^\theta = U''\boldsymbol{s}$. The Hamiltonian H^θ in equation (A13) gives

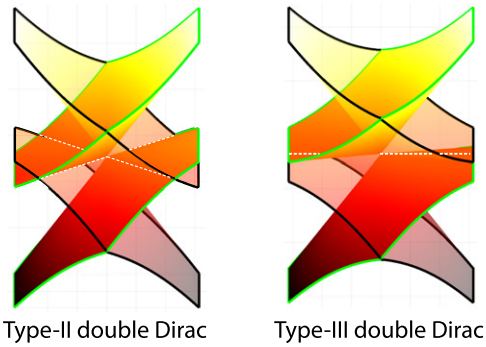

Figure A2. Type-II double Dirac cone when $\tilde{v} = 1.4$ ($\varepsilon' = 1.05$) and type-III double Dirac cone when $\tilde{v} = 1$ ($\varepsilon' = 0.75$). The white dashed lines correspond to the Fermi surface.

rise to two decoupled equations, $\mathcal{H}^{\theta}_{\pm}(\delta\boldsymbol{k})s^{\theta}_{\pm} = \Delta\Omega s^{\theta}_{\pm}$. For $m = 0$, H^{θ} is the Hamiltonian of tilted double Dirac cone. For $m \neq 0$, H^{θ} is the anisotropic QSH Hamiltonian.

Appendix C. Type-II and type-III double Dirac cones

According to the Hamiltonian $\mathcal{H}^{\theta}_{\pm}$, the tilt parameter $\tilde{v} = 4|\varepsilon'|/3$ determines the tilted type of the double Dirac cone. Figure A2 shows the type-II and type-III double Dirac cones by tuning ε'.

Appendix D. Pseudo-TRS and Berry curvatures

In a spin-1/2 system, the QSH topological phase is protected by TRS where $T^2 = -1$ guarantees the existence of the Kramers' pair. And a T-invariant Bloch Hamiltonian must satisfy,

$$TH(k_x, k_y)T^{-1} = H(-k_x, -k_y). \tag{A14}$$

Due to its bosonic nature where $T^2 = 1$, the analogies of QSH phase in spinless systems are not protected by the real TRS but a pseudo-TRS is constructed usually by other symmetries, e.g., C_6 in many reported photonic/phononic systems. Next, we show that the effective Hamiltonian of the MGG around the Γ point satisfies the same property as equation (A14) under the C_2 symmetry.

Let us consider the rotation axis along z-axis passing through the midpoint of the center distance of A and B beads. The C_2 operation can be described by a rotation matrix (we ignore z component as its contribution to the Dirac physics around the Γ point is negligible),

$$\mathcal{R}_{\pi} = \begin{bmatrix} \cos\vartheta & -\sin\vartheta \\ \sin\vartheta & \cos\vartheta \end{bmatrix}_{\vartheta=\pi} = \begin{bmatrix} -1 & 0 \\ 0 & -1 \end{bmatrix}. \tag{A15}$$

In addition, sublattices A and B change positions after a 180° rotation,

$$\begin{bmatrix} B \\ A \end{bmatrix} = \mathcal{S}\begin{bmatrix} A \\ B \end{bmatrix}, \quad \mathcal{S} = \begin{bmatrix} 0 & 1 \\ 1 & 0 \end{bmatrix}. \tag{A16}$$

Thus, a C_2 operator is expressed as $\mathcal{C}_{\pi} = \mathcal{S} \otimes \mathcal{R}_{\pi}$. It is easy to prove that the Hamiltonian in equation (A6) satisfies,

$$\mathcal{C}_{\pi}H(\delta k_x, \delta k_y)\mathcal{C}_{\pi}^{-1} = H(-\delta k_x, -\delta k_y). \tag{A17}$$

Compared equations (A14) and (A17), it leads to an important conclusion that the $\mathcal{C}_{\pi}$ acting on the effective Hamiltonian of the MGG has the same property as T on the Bloch Hamiltonian of a spin-1/2 system. Under the C_2 rotation, the Hamiltonian is invariant. In this way, pseudo-TRS T_{P} can be constructed based on the $\mathcal{C}_{\pi}$ as long as it holds $T_{\mathrm{P}}^2 = -1$ and commutes with $\mathcal{C}_{\pi}$. Therefore, one pseudo-TRS is constructed as $T_{\mathrm{P}} = -\mathrm{i}\sigma_0 \otimes \sigma_y\mathcal{K}$ ($\mathcal{K}$ is complex conjugation). It is possible to check that $T_{\mathrm{P}}^2 = -1$ and $[\mathcal{C}_{\pi}, T_{\mathrm{P}}] = 0$. One should also notice that the C_2 rotation holds $(\delta k_x, \delta k_y) \to (-\delta k_x, -\delta k_y)$, $H(\delta k_x, \delta k_y) \to H(-\delta k_x, -\delta k_y)$ with the rotating axis must passing through the Γ point of the BZ center. Thus, the discussion here is valid around the Dirac point at the high symmetry Γ point.

The Berry curvature around the Dirac point can be calculated using the eigenmodes of $\mathcal{H}^{\theta}_{\pm}$. Taking $\mathcal{H}^{\theta}_{+}$ as an example, its eigenvalues are $\lambda_{\pm} = \pm\sqrt{V_+^2(\delta k_x^2 + \delta k_y^2) + m^2}$, and the corresponding eigenmodes can

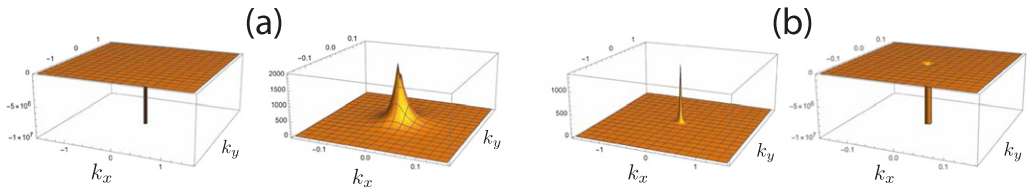

Figure A3. Berry curvatures calculated from the eigenvectors of the Hamiltonian $\mathcal{H}^{\theta}_{\pm}$. They show a Z_2 invariant around the BZ center where $q_x \sim 0$ and $q_y \sim 0$. (a) Berry curvatures of lower cone. (b) Berry curvatures of upper cone.

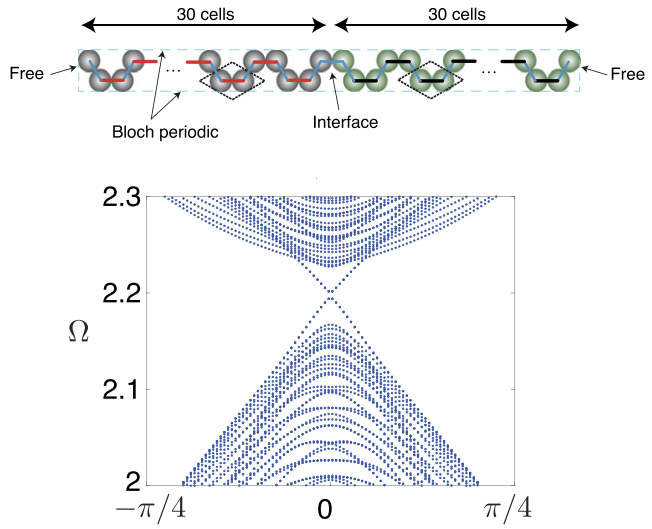

Figure A4. Top: schematics of a strip used to calculate the edge wave dispersion. Bottom: the corresponding wave spectra of the strip.

be chosen as,

$$\boldsymbol{v}_{\pm} = \begin{bmatrix} \dfrac{V_+(\delta k_x - \mathrm{i}\delta k_y)}{\lambda_{\pm} - m} \\ 1 \end{bmatrix}. \tag{A18}$$

The definition of the Berry connection is given by, $\boldsymbol{A} = i\langle \boldsymbol{v}_{\pm}|\nabla_{\boldsymbol{k}}|\boldsymbol{v}_{\pm}\rangle$, and the Berry curvature by $\boldsymbol{B} = \nabla_{\boldsymbol{k}} \times \boldsymbol{A}$. Therefore, based on equation (A18), we can numerically calculated the Berry curvatures around the Dirac frequency. In figure A3, we show the Berry curvatures of the four branches around the Γ point. The Chern number is defined as the integral of the Berry curvature of the same spin over the Brillouin zone. Since our granular system exhibits pseudo-spin and pseudo-time-reversal symmetry, then the pseudo-spins up and down have independent Chern integers N_+ and N_-, which are -1, $+1$ for the two-fold degeneracy of lower cone, and $+1$, -1 for the two-fold degeneracy of upper cone based on the Berry curvatures in figure A3. Due to the real TRS, the overall Chern number ($N = N_+ + N_-$) is always zero for each two-fold degeneracy. However, the spin Chern number, defined as $N_s = N_+ - N_-$, is nonzero due to pseudo-time-reversal symmetry. This leads to a Z_2 invariant in the granular graphene.

Appendix E. Edge wave spectra

As shown in figure A4, we consider a strip consisting of 60 cells with the zigzag interface in the middle. The direction perpendicular to the strip is treated as periodic. Since each particle has three DOFs, we can write down in total $3 \times 2 \times 60$ equations of motion including the interface configuration. Combining the boundary condition of free edges on the two ends of the strip, the spectra including bulk, interface and free edge modes can be derived, see the bottom panel of figure A4. In main text, figures 4(a) and (b) are the projections of bulk modes to the VZI and IZI based on the bulk Hamiltonian. To be more specific, all the bulk modes at each point of the BZ can be obtained from the bulk Hamiltonian, and they are projected to the directions along VZI or IZI when we focus on the waves along the interfaces. The edge wave dispersions for the two interfaces are obtained by further solving the boundary condition of the interfaces. By

comparing the results of the VZI in figure 4(a) with the one in figure A4, it is clear that they are consistent to each other. There, we highlight the interface branches as blue and red, while we mark the bulk region in grey.

ORCID iDs

Li-Yang Zheng https://orcid.org/0000-0003-0438-0488
Georgios Theocharis https://orcid.org/0000-0003-2984-4197
Romain Fleury https://orcid.org/0000-0002-9486-6854
Vincent Tournat https://orcid.org/0000-0003-4497-5742

References

[1] Hasan M Z and Kane C L 2010 *Rev. Mod. Phys.* **82** 3045
[2] Qi X-L and Zhang S-C 2011 *Rev. Mod. Phys.* **83** 1057
[3] Ando Y and Fu L 2015 *Annu. Rev. Condens. Matter Phys.* **6** 361
[4] Yan B and Felser C 2017 *Annu. Rev. Condens. Matter Phys.* **8** 337
[5] Sato M and Ando Y 2017 *Rep. Prog. Phys.* **80** 076501
[6] Rechtsman M C, Zeuner J M, Plotnik Y, Lumer Y, Podolsky D, Dreisow F, Nolte S, Segev M and Szameit A 2013 *Nature* **496** 196
[7] Brendel C, Peano V, Painter O and Marquardt F 2018 *Phys. Rev.* B **97** 020102
[8] Yves S, Fleury R, Berthelot T, Fink M, Lemoult F and Lerosey G 2017 *Nat. Commun.* **8** 16023
[9] Haldane F D M 1988 *Phys. Rev. Lett.* **61** 2015
[10] Lu J, Qiu C, Deng W, Huang X, Li F, Zhang F, Chen S and Liu Z 2018 *Phys. Rev. Lett.* **120** 116802
[11] Kane C L and Mele E J 2005 *Phys. Rev. Lett.* **95** 343
[12] Kane C L and Mele E J 2005 *Phys. Rev. Lett.* **95** 226801
[13] Bernevig B A, Hughes T L and Zhang S-C 2006 *Science* **314** 1757
[14] Wang Z, Chong Y, Joannopoulos J D and Soljacic M 2009 *Nature* **461** 772
[15] Wang P, Lu L and Bertoldi K 2015 *Phys. Rev. Lett.* **115** 104302
[16] Yang Z, Gao F, Shi X, Lin X, Gao Z, Chong Y and Zhang B 2015 *Phys. Rev. Lett.* **114** 114301
[17] Zhang X, Xiao M, Cheng Y, Lu M-H and Christensen J 2018 *Commun. Phys.* **1** 97
[18] Liu Y, Lian C-S, Li Y, Xu Y and Duan W 2017 *Phys. Rev. Lett.* **119** 255901
[19] Wu L-H and Hu X 2015 *Phys. Rev. Lett.* **114** 223901
[20] Ma T, Khanikaev A B, Mousavi S H and Shvets G 2015 *Phys. Rev. Lett.* **114** 127401
[21] He C, Ni X, Ge H, Sun X-C, Chen Y B, Lu M-H, Liu X-P and Chen Y-F 2016 *Nat. Phys.* **12** 1124
[22] Goerbig M O, Fuchs J N, Montambaux G and Piechon F 2008 *Phys. Rev.* B **78** 1006
[23] Goerbig M O 2011 *Rev. Mod. Phys.* **83** 1193
[24] Oliva-Leyva M and Naumis G G 2016 *Phys. Rev.* B **93** 035439
[25] Kawarabayashi T, Hatsugai Y, Morimoto T and Aoki H 2012 *Int. J. Mod. Phys.: Conf. Ser.* **11** 145–50
[26] Huang Z-M, Zhou J and Shen S-Q 2017 *Phys. Rev.* B **95** 1280
[27] Isobe H and Nagaosa N 2016 *Phys. Rev. Lett.* **116** 205
[28] Lu H-Y, Cuamba A S, Lin S-Y, Hao L, Wang R, Li H, Zhao Y and Ting C S 2016 *Phys. Rev.* B **94** 195423
[29] Hirata M, Ishikawa K, Miyagawa K, Tamura M, Berthier C, Basko D, Kobayashi A, Matsuno G and Kanoda K 2016 *Nat. Commun.* **7** 12666
[30] Li D, Rosenstein B, Shapiro B Y and Shapiro I 2017 *Phys. Rev.* B **95** 094513
[31] Noh H-J, Jeong J, Cho E-J, Kim K, Min B I and Park B-G 2017 *Phys. Rev. Lett.* **119** 016401
[32] Soluyanov A A, Gresch D, Wang Z, Wu Q, Troyer M, Dai X and Bernevig B A 2015 *Nature* **527** 495
[33] Huang L *et al* 2016 *Nat. Mater.* **15** 1155
[34] Deng K *et al* 2016 *Nat. Phys.* **12** 1105
[35] Wang H-X, Chen Y, Hang Z H, Kee H-Y and Jiang J-H 2017 *npj Quantum Mater.* **2** 54
[36] Pyrialakos G G, Nye N S, Kantartzis N V and Christodoulides D N 2017 *Phys. Rev. Lett.* **119** 113901
[37] Hu C *et al* 2018 *Phys. Rev. Lett.* **121** 024301
[38] Liu H, Sun J-T, Cheng C, Liu F and Meng S 2018 *Phys. Rev. Lett.* **120** 237403
[39] Huang H, Jin K-H and Liu F 2018 *Phys. Rev.* B **98** 121110
[40] Milicevic M *et al* 2019 *Phys. Rev.* X **9** 031010
[41] Makwana M, Craster R and Guenneau S 2019 *Opt. Express* **27** 16088
[42] Makwana M P and Craster R V 2018 *Phys. Rev.* B **98** 235125
[43] Chan C-K, Lindner N H, Refael G and Lee P A 2017 *Phys. Rev.* B **95** 041104
[44] Steiner J, Andreev A and Pesin D 2017 *Phys. Rev. Lett.* **119** 036601
[45] Ferreiros Y, Zyuzin A A and Bardarson J H 2017 *Phys. Rev.* B **96** 115202
[46] Nguyen V H and Charlier J-C 2018 *Phys. Rev.* B **97** 235113
[47] Zhang S-H and Yang W 2018 *Phys. Rev.* B **97** 235440
[48] de Gail R, Fuchs J N, Goerbig M O, Piechon F and Montambaux G 2012 *Physica* B **407** 1948
[49] Merkel A, Tournat V and Gusev V 2011 *Phys. Rev. Lett.* **107** 225502
[50] Allein F, Tournat V, Gusev V and Theocharis G 2016 *Appl. Phys. Lett.* **108** 161903
[51] Hiraiwa M, Ghanem M A, Wallen S P, Khanolkar A, Maznev A A and Boechler N 2016 *Phys. Rev. Lett.* **116** 198001
[52] Job S, Santibanez F, Tapia F and Melo F 2008 *Ultrasonics* **48** 506
[53] Chen Y, Liu X and Hu G 2019 *J. Mech. Phys. Solids* **122** 54
[54] Zheng L-Y, Theocharis G, Tournat V and Gusev V 2018 *Phys. Rev.* B **97** 060101
[55] Zheng L-Y, Allein F, Tournat V, Gusev V and Theocharis G 2019 *Phys. Rev.* B **99** 184113
[56] Chen H, Nassar H, Norris A N, Hu G K and Huang G L 2018 *Phys. Rev.* B **98** 094302

[57] Brendel C, Peano V, Painter O J and Marquardt F 2017 *Proc. Natl Acad. Sci.* **114** E3390–5
[58] Wen X, Qiu C, Qi Y, Ye L, Ke M, Zhang F and Liu Z 2019 *Nat. Phys.* **15** 352–6
[59] Lado J L, Garcia-Martinez N and Fernandez-Rossier J 2015 *Synth. Met.* **210** 56